PNAS

Supporting Information

Biogenic Carbon Pool Production Maintains the Southern Ocean Carbon Sink

Yibin Huang[1.2], Andrea J. Fassbender[2,1*], Seth M. Bushinsky[3]

[1]Department of Ocean Sciences, University of California, Santa Cruz, CA, USA, 95064
[2]NOAA/OAR Pacific Marine Environmental Laboratory, Seattle, WA, USA, 98115
[3]Department of Oceanography, University of Hawaii at Mānoa, Honolulu, HA, USA, 96822

*Correspondence to: A. J. Fassbender, andrea.j.fassbender@noaa.gov

This PDF file includes:

Supplementary text 1 to 1.8;

Figure S1 to S24;

Table S1 to S3;

SI References

Supplementary Text

1.1 Constraining the C:N Ratio of Dissolved Organic Matter ($C:N_{DOM}$) Production

$C:N_{DOM}$ is constrained using a recently published compilation of global shipboard observations (Hansell et al., 2021; **Fig. S18a**) that includes concurrent measurements of dissolved organic carbon (DOC), total dissolved nitrogen (TDN), and inorganic nitrogen (IN: including nitrate and nitrite). Dissolved organic nitrogen (DON) is computed by subtracting IN from TDN. In seawater, a considerable fraction of TDN is attributed to IN, particularly in high-latitude regions. Thus, the DON values derived by differencing two large values may be subject to a significant error. Unfortunately, accuracies for TDN and IN are not reported in the compiled dataset. We use an analytical error of 4% for TND and 2% for IN measurements to approximate the propagated error associated with our DON estimate (σ_{DON}, **Eq. S7**):

$$\sigma_{DON} = \sqrt{(TND \times 0.04)^2 + (IN \times 0.02)^2} \quad \textbf{Eq. S7}$$

We discard all DON values below σ_{DON}.

Since a large fraction of DOM is refractory (1), the C:N ratio of the bulk DOM pool does not reflect the labile DOM production ratio. Thus, we estimate the $C:N_{DOM}$ for labile DOM production using the seasonal DOC and DON inventory changes. Since the DOM seasonal cycle is rarely resolved (i.e., there are few wintertime observations), we use two approaches to infer the wintertime DOM value (DOM_{winter}) using summertime DOM (DOM_{summer}) observations. The first method is to set DOM_{winter} to the mean of DOM_{summer} values above the annual maximum MLD (MLD_{max}) following Baetge*, et al.* (2) (**Eq. S8**):

$$DOM_{winter} = \frac{\int_0^{MLD_{max}} DOM_{summer}\, dz}{MLD_{max}} \quad \textbf{Eq. S8}$$

where MLD_{max} is determined using an existing monthly Argo climatology product (3). A visual example of this method is shown **Fig. S21.** The second method is to assume that DOM_{winter} is equivalent to the DOM_{summer} profile concentration at the base of annual MLD_{max} (4). After estimating DOM_{winter}, we can calculate the seasonal change in DOC and DON within z_{eu} to quantify $C:N_{DOM}$ (**Eq. S9**):

$$C:N_{DOM} = \frac{\overbrace{\int_0^{Zeu} DOC_{summer}\, dz - Zeu \times DOC_{winter}}^{\Delta DOC}}{\underbrace{\int_0^{Zeu} DON_{summer}\, dz - Zeu \times DON_{winter}}_{\Delta DON}} \quad \textbf{Eq. S9}$$

Before averaging the $C:N_{DOM}$ values into 5° meridional bins, we remove implausible values (e.g., <5 or >25) that we attribute to unresolved horizontal advection or EP effects. The meridional patterns of $C:N_{DOM}$ derived from the two DOM_{winter} reconstruction approaches generally agree within their uncertainties (**Fig. S18b**). In this study, we use the $C:N_{DOM}$ values derived from the Baetge*, et al.* (2) approach as the subsequent carbon pool partitioning results exhibit better agreement with ship-board observations (**Fig. 2d in the main text**).

1.2 Compilation of Shipboard Measurements of Sinking Particle Flux

We compile published shipboard observations of POC and PIC sinking flux (F_{POC} and F_{PIC}) determined by ^{234}Th-^{238}U disequilibrium in the SO during the productive season (**Fig. S20;** Henson*, et al.* (5), Le Moigne*, et al.* (6), Rosengard*, et al.* (7)). In these compiled dataset, F_{PIC} is estimated from F_{POC} multiplied by the PIC:POC ratio determined from contemporaneous observations of suspended particles (7). To maintain a consistent integration depth, we scale the F_{POC} and F_{PIC} values measured at different depth horizons to the base of z_{eu} using the Martin Curve and applying a global average attenuation coefficient (b) of 0.84 (8). The z_{eu} normalized F_{POC} and F_{PIC} values are then averaged into 5° meridional bins. Finally, the seasonal flux is inferred as F_{POC} multiplied by the average number of days in the productive season at each latitude band (**Fig. S1b**), assuming a steady flux over the course of the productive season.

1.3 Residual Potential Nitrate Growth Rate and Dissolved Iron

We analyze the meridional pattern of Residual Potential Nitrate Growth (RNPG, (9)) and dissolved iron to gain insight into the environmental conditions that may favor coccolithophore blooms. RNPG is an index describing the residual potential growth rate for nitrate-dependent algae ($\mu_{NO_3^-}$) relative to silicate-dependent algae (μ_{Si}), under the observed nutrient conditions (9, 10) (**Eq. S15**):

$$\mathrm{RNPG} = \mu_{NO_3^-} - \mu_{Si} \quad \textbf{Eq. S15}$$

The sign of RNPG indicates which type of algal group is expected to outcompete the other, assuming trace metal limitation is relieved. $\mu_{NO_3^-}$ can be modeled as the Michaelis-Menten formulation (**Eq. S16**):

$$\mu_{NO_3^-} = \mu_{NO_3^-\_max} \times \frac{NO_3^-}{K_{NO_3^-\_max} + NO_3^-} \quad \textbf{Eq. S16}$$

where $\mu_{NO_3^-\_max}$ represents the maximum nitrate-dependent growth rate in the absence of substrate limitation, $K_{NO_3^-\_max}$ is the half-saturation coefficient for the growth, and NO_3^- is the seawater concentration from float measurements. Unlike with NO_3^-, it is thought that phytoplankton are unable to fully exhaust seawater silicate (Si). Thereby, a residual Si term (Si_0) is added in the μ_{Si} parameterization as follows (**Eq. S17**):

$$\mu_{Si} = \mu_{Si\_max} \times \frac{Si - Si_0}{K_{Si\_max} + Si_0} \quad \textbf{Eq. S17}$$

where Si_0 is set to 0.7 umol L^{-1} (9). We estimate seawater Si along the float trajectory using the CANYON-B algorithm (11). The maximum growth and half-saturation coefficient are dependent on the nutrient condition, which can be modeled as a function of substrate concentration (S, corresponding to seawater NO_3^- and Si concentration in our study, **Eq. S18, and Eq. S19**):

$$\mu_{S\_max} = \frac{S}{S+2} \times 3 \quad \textbf{Eq. S18}$$

$$K_S = \frac{S}{S+3} \times 5.5 \quad \textbf{Eq. S19}$$

Dissolved iron concentrations are extracted from a gridded, global, monthly climatology product that was created using machine learning to gap fill shipboard observations (12). We interpolate the dissolved iron product in 3-dimensions (location, time, and sampling depth) to align with each float profile before averaging the result into 5° meridional bins for comparison with our PIC production estimates (**Fig. S7**).

1.4 Annual CO_2 Flux Estimate in the Southern Ocean and Comparison with Prior Studies

Our float-based estimate of the annual Southern Ocean (south of 35°S) carbon sink (F_{CO_2}; -0.43 ± 0.14 Pg C yr^{-1}; where negative values indicate ocean carbon uptake) is larger in magnitude than prior float-based estimates (-0.08 ± 0.55 Pg C yr^{-1}, Gray, *et al*. (13), and -0.35 ± 0.19 Pg C yr^{-1}, Bushinsky, *et al*. (14)), indicating a stronger CO_2 sink. This is somewhat surprising because, unlike prior studies that applied a pH-dependent pH adjustment to quality-controlled pH values that yields lower pCO_2 estimates, we expected to find a weaker annual CO_2 sink in the Southern Ocean. However, it is worth noting that prior studies relied on float observations from May 2014 to April 2017, reflecting significantly fewer observations than our study. To test the importance of data density, we recalculate F_{CO_2} using only the float observations from May 2014 to April 2017 and replicating all flux calculation procedures from prior studies (13) except for the pH-dependent pH adjustment. This includes the use of ERA-interim wind speed and the division of the Southern Ocean into five frontal regions, with the PAZ further partitioned into the PFZ and ASZ. We find the SO to be a source of CO_2 to the atmosphere (+0.28 ± 0.076 Pg C yr^{-1}), matching expectations. Recent finding by Stammerjohn, *et al*. (15) similarly found that greater data coverage from the current, larger float array leads to an elevated SO CO_2 sink estimate. Therefore, the difference in data coverage and/or inter-annual variability could be contributing to the larger SO CO_2 uptake found in our work using float observations from 2014 to 2021.

Notably, our float-based SO F_{CO_2} estimate still suggests a weaker annual sink than estimates derived from shipboard observations upscaled to the entire SO using machine learning techniques (~ -1.1 Pg C yr^{-1} in the south of 35°S) (14, 16, 17). These gap-filled data products have known seasonal sampling biases in their training datasets due to a lack of wintertime observations in high-latitude regions that are anticipated to exhibit strong seasonal CO_2 outgassing (13, 18). A recent study by Long, *et al*. (19), using atmospheric CO_2 gradient observations from aircraft, reported nearly double the CO_2 influx (-0.53 ± 0.23 Pg C yr^{-1}; average over 2009-2018) of our float-based estimate in the region south of 45° S (-0.26 ± 0.07 Pg C yr^{-1}). Further study is needed to reduce the uncertainty in Southern Ocean F_{CO_2} estimates by considering potential discrepancies in methodology, inter-annual variability, and sampling coverage.

1.5 Potential Biases in Float-based POC and PIC Estimates and the Implications in Carbon Pool Partitioning

Float-based POC concentrations ($POC_{b_{bp}}$) in our study are derived from float b_{bp} observations using a global empirical relationship (20). This might not be suitable in regions with coccolithophore blooms (e.g., 47-57 °S in our study, **Fig. S7**) where highly-refractive calcite particles (coccoliths) could lead to elevated b_{bp} signals (9). Such a bias in our $POC_{b_{bp}}$ estimate could distort the magnitude and meridional pattern of net biological production solved from the $POC_{b_{bp}}$ budget $\left(\frac{\partial POC_{b_{bp}}}{\partial t}|_{Bio}\right)$. Further, since the net biological production of suspended PIC $\left(\frac{\partial PIC_{b_{bp}}}{\partial t}|_{Bio}\right)$ is calculated from $\frac{\partial POC_{b_{bp}}}{\partial t}|_{Bio}$ multiplied by the satellite derived surface PIC:POC ratio (***Eq.*** *7* in the main text), $\frac{\partial PIC_{b_{bp}}}{\partial t}|_{Bio}$ will be influenced by the assumption of a constant PIC:POC ratio throughout the euphotic zone column.

Our work focuses on variability in the export potential of distinct biogenic carbon pools ($\frac{\partial DIC}{\partial t}|_{Bio\_POC}, \frac{\partial DIC}{\partial t}|_{Bio\_DOC}, \frac{\partial DIC}{\partial t}|_{Bio\_PIC}$) and the associated particle sinking fluxes (F_{POC} and F_{PIC}). The former relies on linking multiple chemical tracer budgets (***Eq. 4-5* in the main text**), which eliminates the relevance of a potential $POC_{b_{bp}}$ and $PIC_{b_{bp}}$ bias. However, such a bias would propagate into the subsequent computations of F_{POC} and F_{PIC}, which are determined by subtracting $\frac{\partial POC_{b_{bp}}}{\partial t}|_{Bio}$ (or $\frac{\partial PIC_{b_{bp}}}{\partial t}|_{Bio}$) from $\frac{\partial DIC}{\partial t}|_{Bio\_POC}$ (or $\frac{\partial DIC}{\partial t}|_{Bio\_PIC}$). It is worth pointing out that the magnitudes of biological terms solved from suspended particles are one-tenth of the corresponding chemically derived export potential values (**Fig. S22**). Therefore, F_{POC} and F_{PIC} are less sensitive to potential errors in the $POC_{b_{bp\_bio}}$ and $PIC_{b_{bp\_bio}}$ estimates.

1.6 Tracer Budgets

We use a 1-dimensional mass balance model approach to account for processes affecting the time rate of concentration change (mmol m^{-3} d^{-1}) of biologically relevant tracers (DIC, TA, NO_3^-, and $POC_{b_{bp}}$) that are observed by profiling floats within the euphotic zone (z_{eu}) (**Eq. S1**):

$$\frac{dT_{\left(DIC,TA,NO_3^-,POC_{b_{bp}}\right)}}{dt}|_{Obs_{zeu}} = \frac{\partial T_{(DIC)}}{\partial t}|_{Gas_{zeu}} + \frac{\partial T_{\left(DIC,TA,NO_3^-,POC_{b_{bp}}\right)}}{\partial t}|_{Phys_{zeu}} + \frac{\partial T_{\left(DIC,TA,NO_3^-,POC_{b_{bp}}\right)}}{\partial t}|_{EP_{zeu}} + \frac{\partial T_{\left(DIC,TA,NO_3^-,POC_{b_{bp}}\right)}}{\partial t}|_{Bio_{zeu}} \quad \textbf{Eq. S1}$$

where subscripts on the right-hand side represent air-sea gas exchange (Gas), physical transport and mixing (Phys), evaporation and precipitation (EP), and biological activity (Bio), respectively. The computation of air-sea gas exchange for the dissolved inorganic carbon (DIC) budget is described in the methods section.

When z_{eu} is deeper than the mixed layer depth (MLD; defined by a temperature increase of 0.2 °C relative to the 10 m temperature, following de Boyer Montégut*, et al.* (21), physical transport and mixing at the base of z_{eu} consists of diapycnal diffusion and wind-induced Ekman pumping (shown here for DIC, **Eq. S2**):

$$\frac{\partial \mathrm{DIC}}{\partial t}\Big|_{\mathrm{Phys}_{z_{eu}}} = (\underbrace{K_{z\_z_{eu}} \times \frac{\partial \mathrm{DIC}}{\partial z}\Big|_{z_{eu}}}_{\text{Diapycnal diffusion}} + \underbrace{w_{z_{eu}} \times \int_0^{z_{eu}} \frac{\partial \mathrm{DIC}}{dz}}_{\text{Ekman pumping}})/z_{eu};\ \text{for } z_{eu} > \mathrm{MLD} \qquad \textbf{Eq. S2}$$

where $K_{z\_z_{eu}}$ is the diapycnal diffusivity coefficient, $\frac{\partial \mathrm{DIC}}{\partial z}\Big|_{z_{eu}}$ is the vertical DIC gradient across z_{eu}, $w_{z_{eu}}$ is the Ekman pumping velocity computed from satellite-derived wind stress following Signorini, *et al.* (22), and $\int_0^{z_{eu}} \frac{\mathrm{DIC}}{dz}$ is the depth integrated DIC vertical gradient. In this study, we set K_Z to 10^{-4} m s^{-2} at the base of the mixed layer (23) with an exponential decay to the background value of 10^{-5} m s^{-2} over 20 m following 1/e scaling (24). We recognize the present choice of K_Z is somewhat arbitrary. Nevertheless, our analysis focuses on the spring/summer season when the upper layer water column is stratified and stable. Therefore, we believe the diapycnal diffusion during this period is minimal and the magnitude of K_Z has a limited effect on the biological term estimate.

During periods when the MLD exceeds z_{eu}, $\frac{\partial \mathrm{DIC}}{\partial t}\Big|_{\mathrm{Phys}_{z_{eu}}}$ is scaled from the physical transport and mixing at the base MLD $\left(\frac{\partial \mathrm{DIC}}{\partial t}\Big|_{\mathrm{Phys}_{\mathrm{MLD}}}\right)$ by assuming the impacts of physical transport and mixing occurring at the base of MLD will be equally distributed throughout the entire mixed water column (**Eq. S3**):

$$\frac{\partial \mathrm{DIC}}{\partial t}\Big|_{\mathrm{Phys}_{z_{eu}}} = \frac{\partial \mathrm{DIC}}{\partial t}\Big|_{\mathrm{Phys}_{\mathrm{MLD}}} \times \frac{z_{eu}}{\mathrm{MLD}};\ \text{for } z_{eu} < \mathrm{MLD} \qquad \textbf{Eq. S3}$$

Compared with $\frac{\partial \mathrm{DIC}}{\partial t}\Big|_{\mathrm{Phys}_{z_{eu}}}$ shown in **Eq. S2**, $\frac{\partial \mathrm{DIC}}{\partial t}\Big|_{\mathrm{Phys}_{\mathrm{MLD}}}$ encompasses an additional term, entrainment, to account for tracer changes induced by MLD changes (**Eq. S4**):

$$\frac{\partial \mathrm{DIC}}{\partial t}\Big|_{\mathrm{Phys}_{\mathrm{MLD}}} = (\underbrace{K_{z_{\mathrm{MLD}}} \times \frac{\partial \mathrm{DIC}}{\partial z}\Big|_{\mathrm{MLD}}}_{\text{Diapycnal diffusion}} + \underbrace{w_{MLD} \times \int_0^{\mathrm{MLD}} \frac{\partial \mathrm{DIC}}{dz}}_{\text{Ekman pumping}} + \underbrace{(\mathrm{DIC}_{\mathrm{base}} - \overline{\mathrm{DIC}_{\mathrm{MLD}}}) \times \frac{\partial \mathrm{MLD}}{dt}}_{\text{Entrainment}})/\mathrm{MLD}$$

Eq. S4

Entrainment can be modeled as a product of the MLD time rate of change $\left(\frac{\partial \mathrm{MLD}}{dt}\right)$ and the difference between the average DIC concentration within MLD ($\overline{\mathrm{DIC}_{\mathrm{MLD}}}$) and DIC concentration at the base of MLD ($\mathrm{DIC}_{\mathrm{base}}$). The entrainment term is set to zero when the MLD shoals $\left(\frac{\partial \mathrm{MLD}}{dt} < 0\right)$.

The evaporation and precipitation term is quantified using the ratio of tracer to salinity at initial time t1 $\left(\frac{T_{(\mathrm{DIC,TA,NO_3^-,POC_{b_{bp}}})}}{\mathrm{Sal}}\Big|_{t1}\right)$ multiplied by the salinity time rate of change due to EP $\left(\frac{\partial \mathrm{Sal}}{\partial t}\Big|_{\mathrm{EP}_{z_{eu}}}\right)$ (**Eq. S5**):

$$\frac{\partial T_{(\mathrm{DIC,TA,NO_3^-,POC_{b_{bp}}})}}{\partial t}\Big|_{\mathrm{EP}_{z_{eu}}} = \frac{\partial \mathrm{Sal}}{\partial t}\Big|_{\mathrm{EP}_{z_{eu}}} \times \frac{T_{(\mathrm{DIC,TA,NO_3^-,POC_{b_{bp}}})}}{\mathrm{Sal}}\Big|_{t1} \qquad \textbf{Eq. S5}$$

$\frac{\partial Sal}{\partial t}|_{EP_{z_{eu}}}$ is computed from the difference between observed salinity changes and estimated physically driven salinity changes (**Eq. S6**):

$$\frac{\partial Sal}{\partial t}|_{EP_{z_{eu}}} = \frac{\partial Sal}{\partial t}|_{obs_{z_{eu}}} - \frac{\partial Sal}{\partial t}|_{Phys_{z_{eu}}} \quad \textbf{Eq. S6}$$

After accounting for abiotic terms, the biological term can be calculated as a residual.

1.7 Reconstruction of DIC and TA for Different Productivity Scenarios

To assess the role of biology in maintaining the Southern Ocean carbon sink, we reconstruct DIC and TA time series for different scenarios of modified productivity: only organic matter production and zero biological production (abiotic). Float-derived DIC values (DIC_{Obs_n}) can be expressed as a sum of the DIC concentration at the start of the productive season (DIC_{Obs_1}) and the time integral of DIC changes from biology $\left(\sum_{day_1}^{day_{n-1}} \frac{\partial DIC}{\partial t}|_{Bio}\right)$, air-sea gas exchange $\left(\sum_{day_1}^{day_{n-1}} \frac{\partial DIC}{\partial t}|_{Gas}\right)$, and other abiotic processes $\left(\sum_{day_1}^{day_{n-1}} \frac{\partial DIC}{\partial t}|_{Other}\right)$ including evaporation/precipitation, and physical transport and mixing (**Eq. S10**):

$$DIC_{Obs\_n} = DIC_{Obs\_1} + \sum_{day_1}^{day_{n-1}} \frac{\partial DIC}{\partial t}|_{Bio} + \sum_{day_1}^{day_{n-1}} \frac{\partial DIC}{\partial t}|_{Gas} + \sum_{day_1}^{day_{n-1}} \frac{\partial DIC}{\partial t}|_{Other} \quad \textbf{Eq. S10}$$

Likewise, the time-series of DIC in the reconstructed, abiotic ocean (DIC_{abio_n}) can be written as follows (**Eq. S11**):

$$DIC_{abiotic\_n} = DIC_{Obs\_1} + \sum_{day_1}^{day_{n-1}} \frac{\partial DIC}{\partial t}|_{Gas\_abiotic} + \sum_{day_1}^{day_{n-1}} \frac{\partial DIC}{\partial t}|_{Other\_abiotic} \quad \textbf{Eq. S11}$$

For simplicity, we assume the "other" terms are equivalent between the observed and reconstructed scenarios ($\sum_{day_1}^{day_{n-1}} \frac{\partial DIC}{\partial t}|_{Other} \approx \sum_{day_1}^{day_{n-1}} \frac{\partial DIC}{\partial t}|_{Other\_abiotic}$), and rearrange DIC_{abio_n} by linking **Eq. S10** with **Eq. S11** (**Eq. S12**, same as **Eq. 12** in the main text):

$$DIC_{abiotic\_n} = DIC_{Obs\_n} - \sum_{day_1}^{day_{n-1}} \frac{\partial DIC}{\partial t}|_{Bio} - \left(\sum_{day_1}^{day_{n-1}} \frac{\partial DIC}{\partial t}|_{Gas} - \sum_{day_1}^{day_{n-1}} \frac{\partial DIC}{\partial t}|_{Gas\_abiotic}\right) \quad \textbf{Eq. S12}$$

As shown in **Eq. S12**, the abiotic DIC time series can be inferred from the float-derived DIC at the corresponding time step, with an adjustment for the time integral of biological production and the gas exchange difference between the two scenarios. A similar approach can be used to derive the abiotic TA time series ($TA_{abiotic\_n}$), which excludes the influence of gas exchange (**Eq. S13, same as Eq. 11** in the main text):

$$TA_{abiotic\_n} = TA_{Obs\_n} - \sum_{day_1}^{day_{n-1}} \frac{\partial TA}{\partial t}|_{Bio} \quad \textbf{Eq. S13}$$

Since TA_{Obs_n} and $\frac{\partial TA}{\partial t}|_{Bio\_n}$ are previously quantified terms, we can directly reconstruct $TA_{abiotic}$ following **Eq. S13**.

The $\frac{\partial DIC}{\partial t}|_{Gas\_abiotic}$ term required to compute $DIC_{abiotic}$ in **Eq. S12** is determined iteratively. For the initial time step (n =1), we assume the DIC and TA concentrations and gas exchange terms are identical between the observed (biotic) and reconstructed (abiotic) ocean ($DIC_{abiotic\_1}$ = DIC_{Obs_1}; $TA_{abiotic\_1}$ = TA_{Obs_1}; $\frac{\partial DIC}{\partial t}|_{Gas\_abiotic\_1} = \frac{\partial DIC}{\partial t}|_{Gas\_1}$). It follows that there is also no difference between the biotic and abiotic gas exchange terms for the subsequent time step (n = 2, **Eq. S14).**

$$DIC_{abiotic\_2} = DIC_{Obs\_2} - \sum_{day_1}^{day_1} \frac{\partial DIC}{\partial t}|_{Bio} - \underbrace{\left(\sum_{day_1}^{day_1} \frac{\partial DIC}{\partial t}|_{Gas} - \sum_{day_1}^{day_1} \frac{\partial DIC}{\partial t}|_{Gas\_abiotic}\right)}_{set\ to\ 0} \quad \textbf{Eq. S14}$$

With $DIC_{abiotic\_2}$ and $TA_{abiotic\_2}$ we can calculate the abiotic seawater partial pressure of CO_2 ($pCO_{2\_sea\_abiotic\_2}$) and the associated air-sea gas exchange ($\frac{\partial DIC}{\partial t}|_{Gas\_abiotic\_2}$). $DIC_{abiotic\_3}$, and all subsequent time steps, can then be computed following **Eq. S12**. Through this procedure, we iteratively reconstruct the time-series of $DIC_{abiotic}$, $pCO_{2\_sea\_abiotic}$, and $\frac{\partial DIC}{\partial t}|_{Gas\_abiotic}$. A visual example of our reconstruction for different productivity scenarios is provided in **Fig. S23**.

We could infer $DIC_{abiotic\_n}$ from $DIC_{abiotic\_n-1} + \frac{\partial DIC}{\partial t}|_{Gas\_abiotic\_n-1}$; however, any biases in the gas exchange estimates would accumulate iteratively, which could pull our abiotic terms far from the starting DIC value. Considering that the gas exchange velocity (k) used to parameterize air-sea CO_2 flux has a ~30% uncertainty (25, 26), we opt for a method that starts with the float-based DIC estimate at each time step to ensure we are not far from reality. This approach also ensures that pCO_2 changes caused by other physical processes, such as horizontal advection, are not unintentionally omitted.

1.8 Exclusion of Additional pH-dependent pH Adjustment to Quality-controlled SOCCOM Float pH for pCO_2 Computation

The calculation of pH from DIC and TA does not always agree well with directly measured pH values, and this bias can exhibit a pH dependency. Such a pH-dependent pH bias has been identified in numerous high-quality shipboard datasets in which at least three carbonate chemistry parameters (including pH) were measured (27-29). In effort to align float-based pCO_2 estimates with pCO_2 values that would be computed from high-quality DIC and TA observations, a pH-dependent pH adjustment (28) has been routinely applied to quality-controlled SOCCOM float pH observations before computing the pCO_2 values provided in SOCCOM data snapshots (https://soccom.princeton.edu/content/data-access). However, implementation of this adjustment is based on the pH-dependent pH bias at 1500 m, which is then applied to the entire profile as an offset. Thus, the pH adjustment is not applied in a pH-dependent manner and does not correct for the issue presented in Williams, *et al.* (28) and Carter, *et al.* (27), Carter, *et al.* (29). Since 2019, a collaborative international effort entitled the Ocean Carbonate System Intercomparison Forum (OCSIF), supported by the U.S. Ocean Carbon and Biogeochemistry Program (https://www.usocb.org/ocean-carbonate-system-intercomparison-forum/), has focused on identifying the origin of the pH-dependent pH bias in high-quality shipboard observations. While efforts remain ongoing, the current OCSIF recommendation is to use the quality-controlled float pH data directly, without any type of additional pH adjustment, for computations of pCO_2.

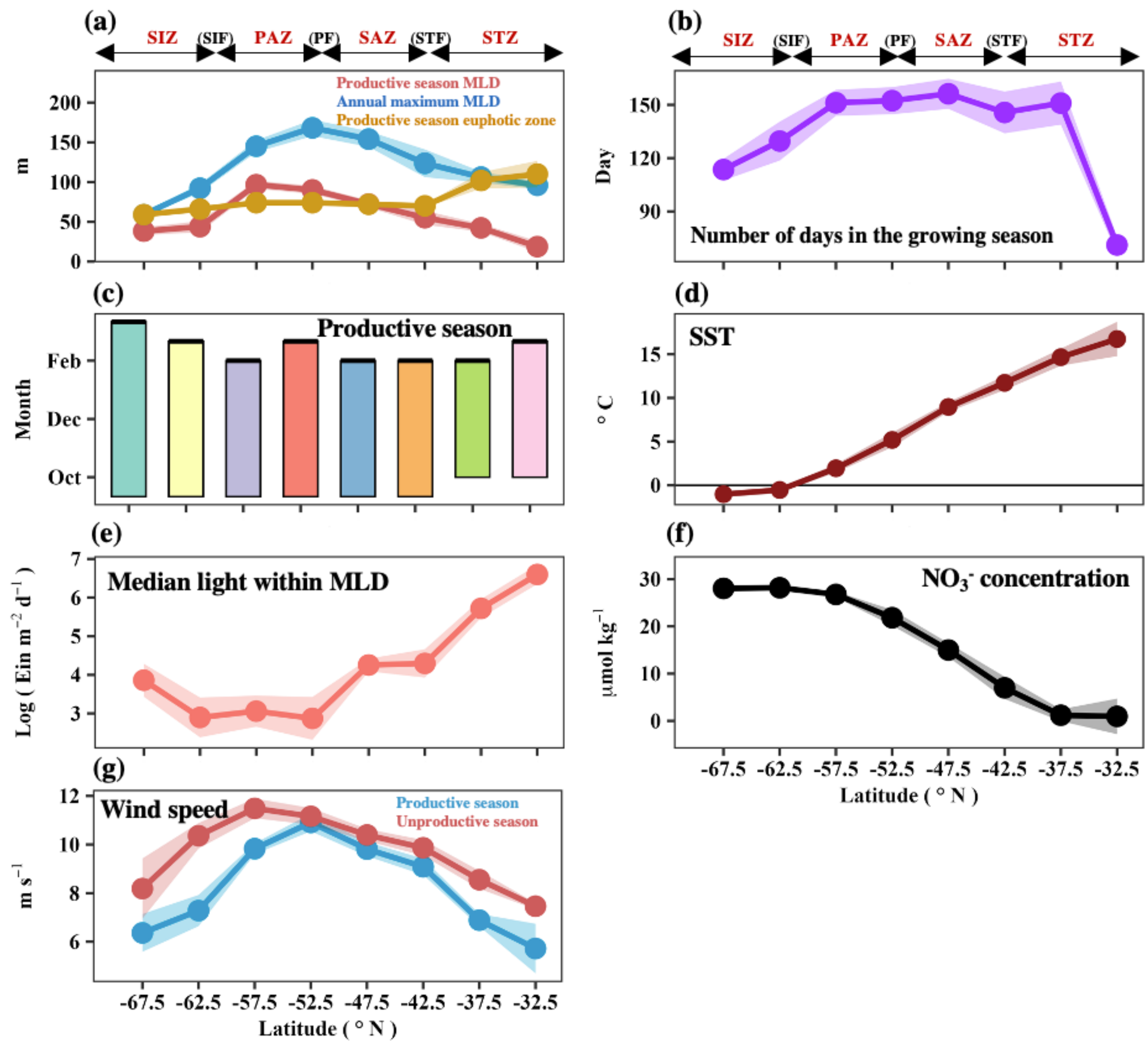

Fig. S1 The meridional patterns of environmental parameters during the Southern Ocean productive season, where shading indicates the propagated error. Median light within mixed layer depth (MLD) is computed based on the remotely sensed surface light field and its attenuation as inferred from float Chl-*a* profiles (30). Note that the frontal labels depicted on the top of the panels indicate rough locations of frontal regions, with a more precise representation appearing in **Fig. S2a**. STF: subtropical front; STZ: subtropical zone; SAZ: subantarctic zone; PF: polar front; PAZ: polar Antarctic zone; SIF: seasonal ice front; SIZ: sea ice zone; SST: sea surface temperature; NO_3^-: nitrate; MLD: mixed layer depth.

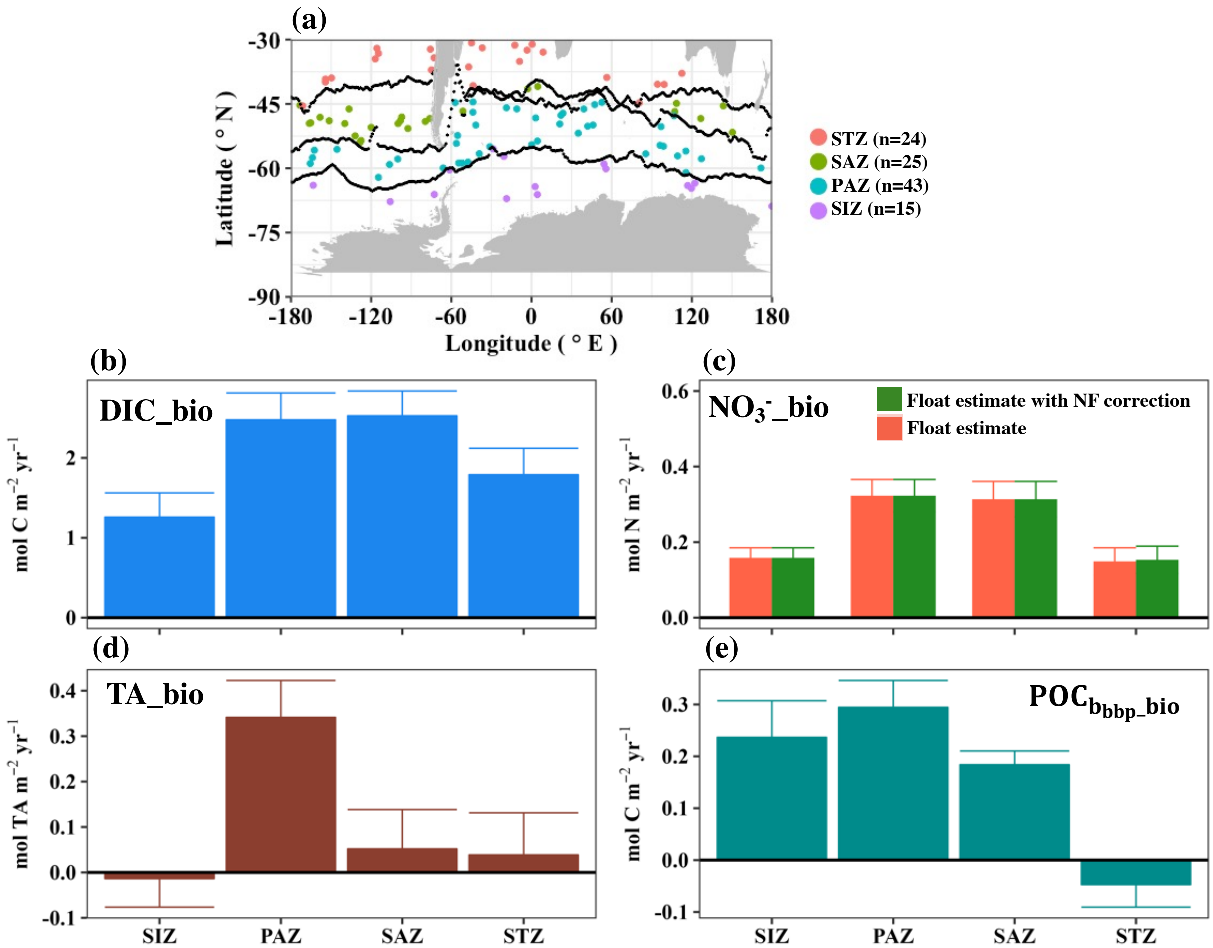

Fig. S2 Net biological production during the Southern Ocean productive season as averaged across the four main frontal zones. (**a**) Mean location of each float for each seasonal production estimate, with frontal zones labeled. Net biological term (bio) results for each frontal region determined from the (**b**) dissolved inorganic carbon (DIC), (**c**) nitrate (NO_3^-), (**d**) total alkalinity (TA), and (**e**) particulate organic carbon (derived from particle backscattering coefficient; $POC_{b_{bp}\_bio}$) tracer budgets. Error bars represent the propagated errors. Numbers in panel a indicate how many independent, float seasonal cycles were evaluated in each frontal zone. Zones as described in **Fig. S1**. NF: nitrogen fixation.

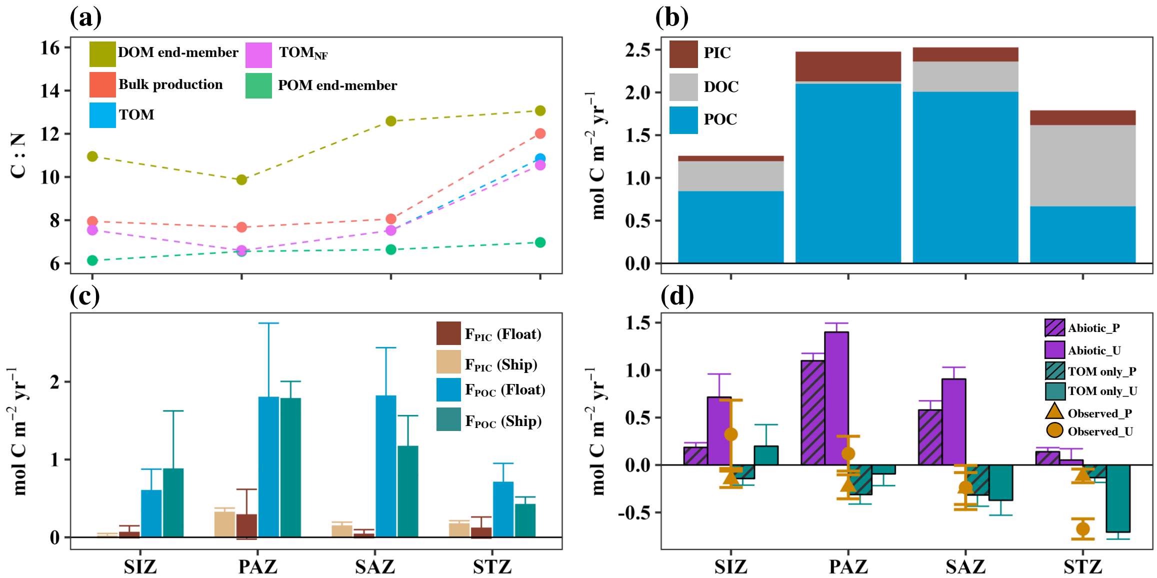

Fig. S3 (**a**) C:N ratio for biological production of different carbon pools, (**b**) magnitude and fraction of distinct carbon pool export potential, (**c**) sinking flux of particulate organic carbon (F_{POC}) and particulate inorganic carbon (F_{PIC}) during the Southern Ocean productive season (P), and (**d**) influence of biology on air-sea CO_2 exchange for different productivity scenarios as averaged over the four main frontal zones. The dissolved organic matter (DOM) and particulate organic matter (POM) end-member C:N ratios are derived from ship-based observations. The bulk biological production, total organic matter (TOM) production, and TOM production with the correction for nitrogen fixation (TOM_{NF}) are derived from float observations and a biogeochemical inverse model. Error bars represent the propagated errors. Positive values in panel d indicate a source of carbon to the atmosphere. Zones as described in **Fig. S1**. DOM: dissolved organic matter; TOM: total organic matter; PIC: particulate inorganic carbon; POM: particulate organic matter; DOC: dissolved organic carbon; POC: particulate organic carbon. Abiotic: reconstructed, abiotic ocean; TOM only: reconstructed ocean with only total organic carbon production; Observed: observed, biotic ocean including both TOM and particulate inorganic carbon production. U: unproductive season.

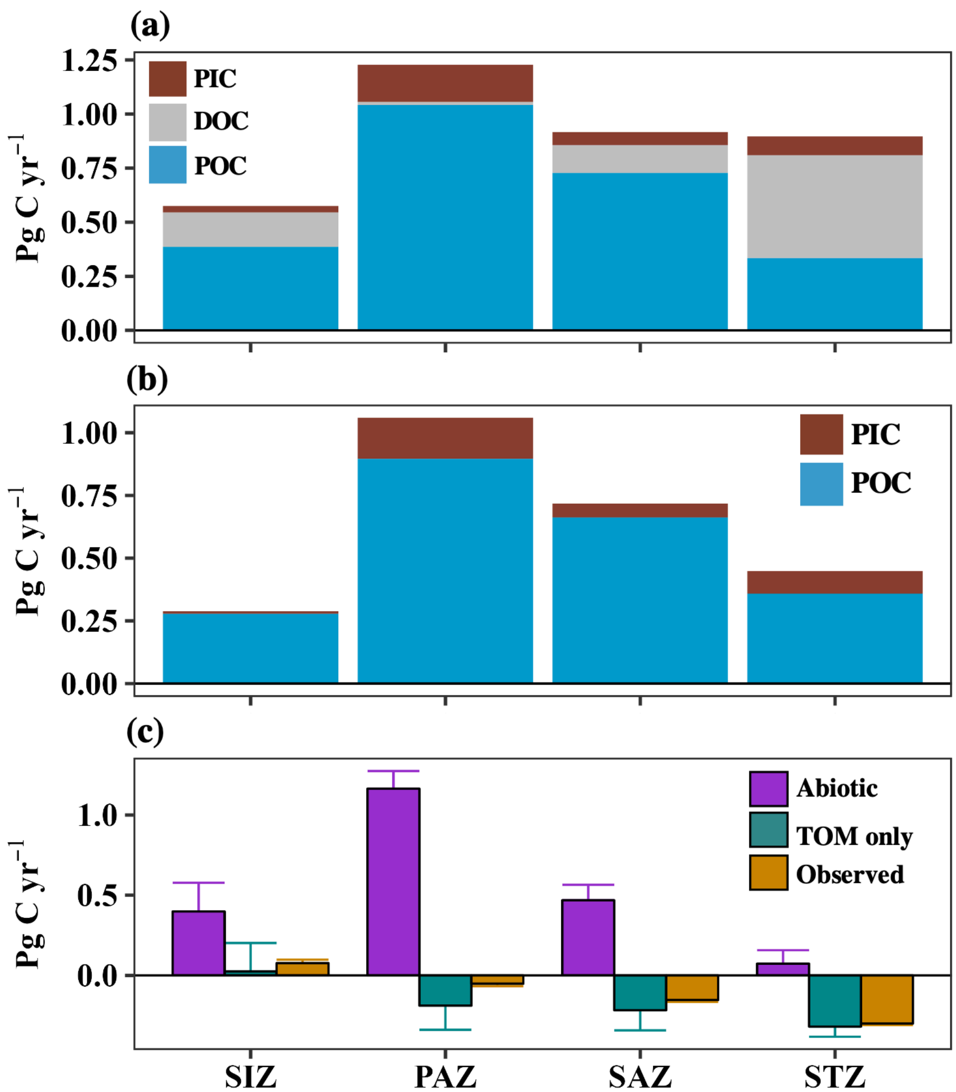

Fig. S4 Area-weighted cumulative annual (**a**) magnitude and (**b**) fraction of distinct carbon pool export potential, and (**c**) influence of biology on annual air-sea CO_2 exchange for different productivity scenarios as averaged over the four main frontal zones. Positive values in panel c indicate a source of carbon to the atmosphere. Error bars represent the propagated errors. Zones as described in **Fig. S1**. TOM: total organic matter; DOC: dissolved organic carbon. Note the annual biological production estimate is scaled from the float-estimated biological production during the productive season using data-constrained model estimates of the fraction of annual biological production that occurs during the productive period at each float location (***Method and Material* in the main text**).

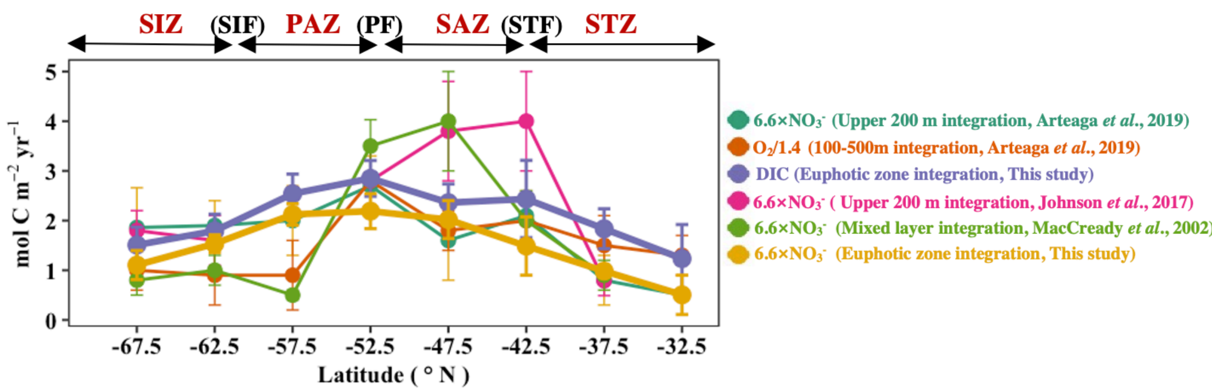

Fig. S5 Comparison of seasonal export potential during the Southern Ocean productive season solved from multiple studies. Export potential values derived from nitrate and oxygen are converted to units of carbon using the Redfield ratio to facilitate comparison. Error bars represent the propagated errors. Zones as described in **Fig. S1**. NO_3^-: nitrate; DIC: dissolved inorganic carbon; O_2: oxygen.

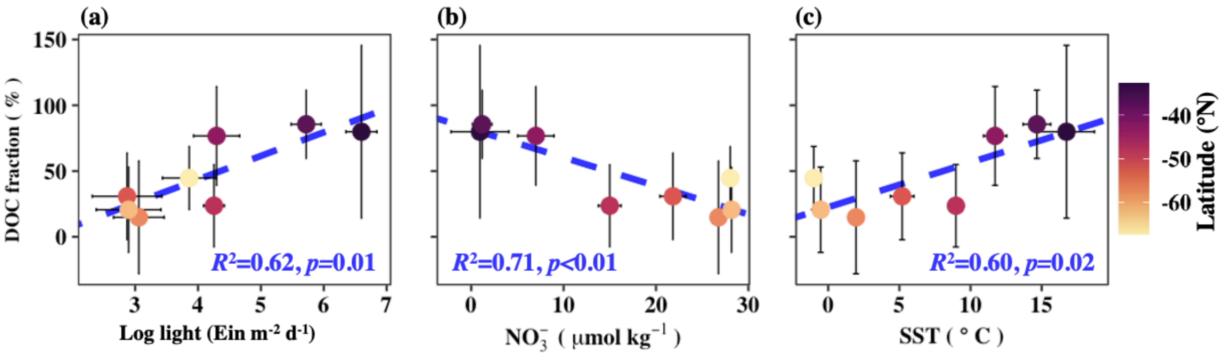

Fig. S6 Relationships between the fraction of total carbon export potential attributed to dissolved organic carbon (DOC) and various environmental parameters during the Southern Ocean productive season. Light availability in panel a refers to the median light field within the mixed layer (**Fig. S1e**). Error bars represent the propagated errors. NO_3^-: nitrate; SST: sea surface temperature.

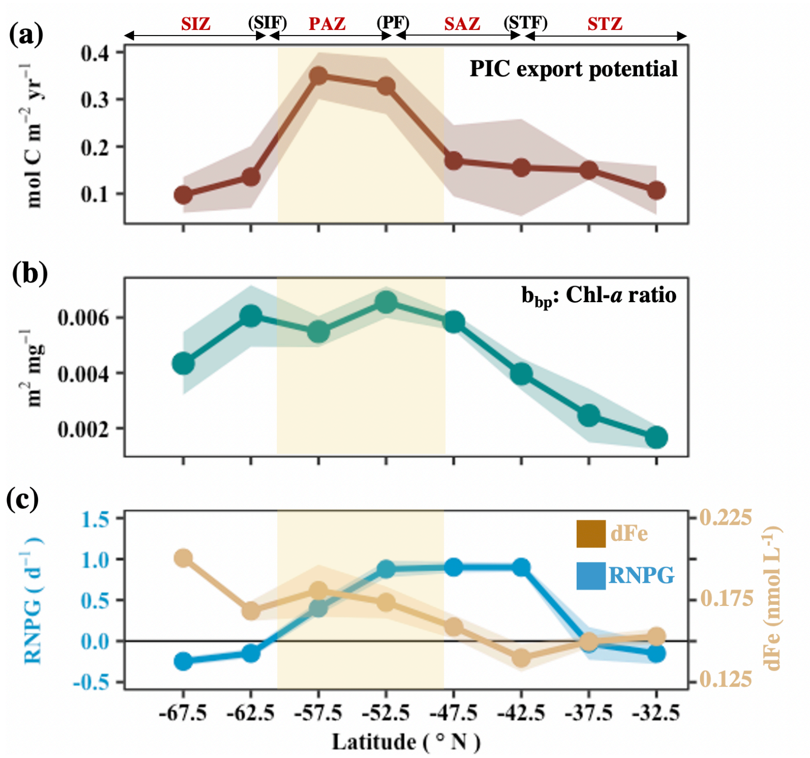

Fig. S7 The meridional pattern of (**a**) seasonal particulate inorganic carbon (PIC) export potential, (**b**) backscattering to Chlorophyll-*a* ratio (b_{bp}:Chl-*a*), and (**c**) dissolved iron (dFe) and residual nitrate potential growth rate (RNPG; detailed description in **Text S1.3**) during the Southern Ocean productive season. Yellow shading highlights the region with enhanced PIC production. Shading on each line reflects the propagated error. Zones as described in **Fig. S1**.

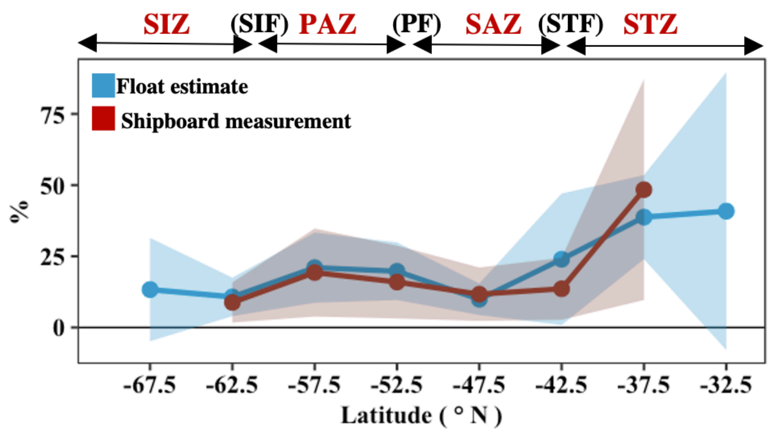

Fig. S8 Meridional pattern (5° bin) of euphotic zone sinking particle rain ratio (F_{PIC}/F_{POC} ×100%) during the Southern Ocean productive season. Shading reflects the propagated error. Zones as described in **Fig. S1**.

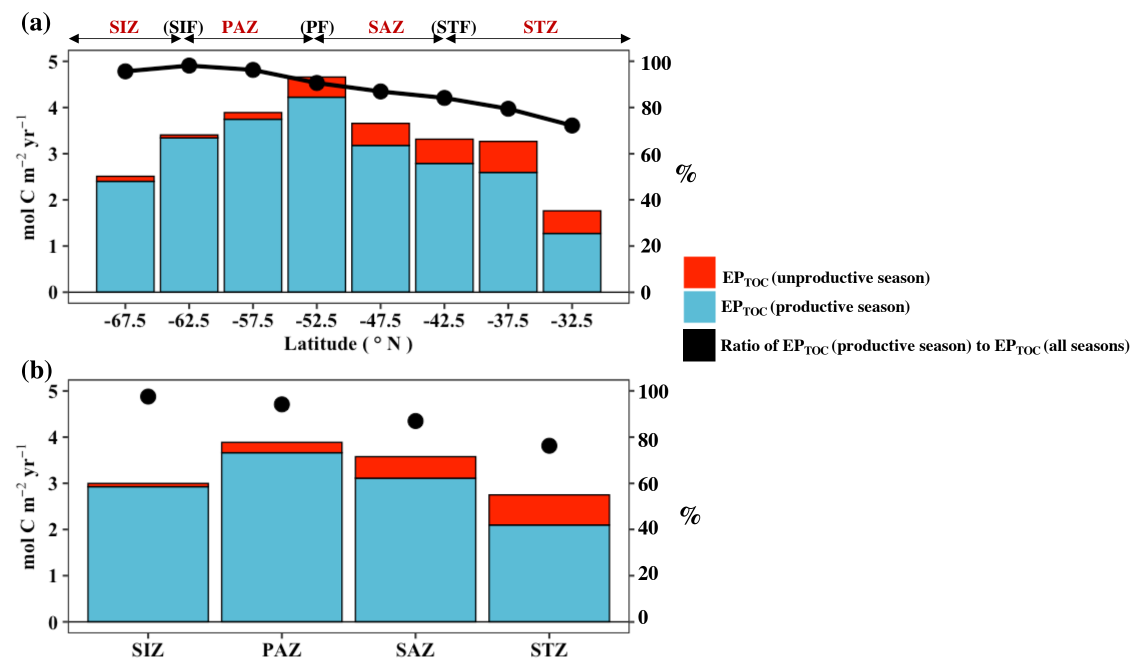

Fig. S9 Year 2008 to 2018 average euphotic zone integrated export potential of total organic carbon (EP_{TOC}) in the Southern Ocean for the productive and unproductive seasons derived from data-constrained biogeochemical Southern Ocean State Estimate (B-SOSE) model output (31). Results are shown for (**a**) 5° latitude bins and (**b**) the four main frontal regions. Frontal regions as described in **Fig. S1**.

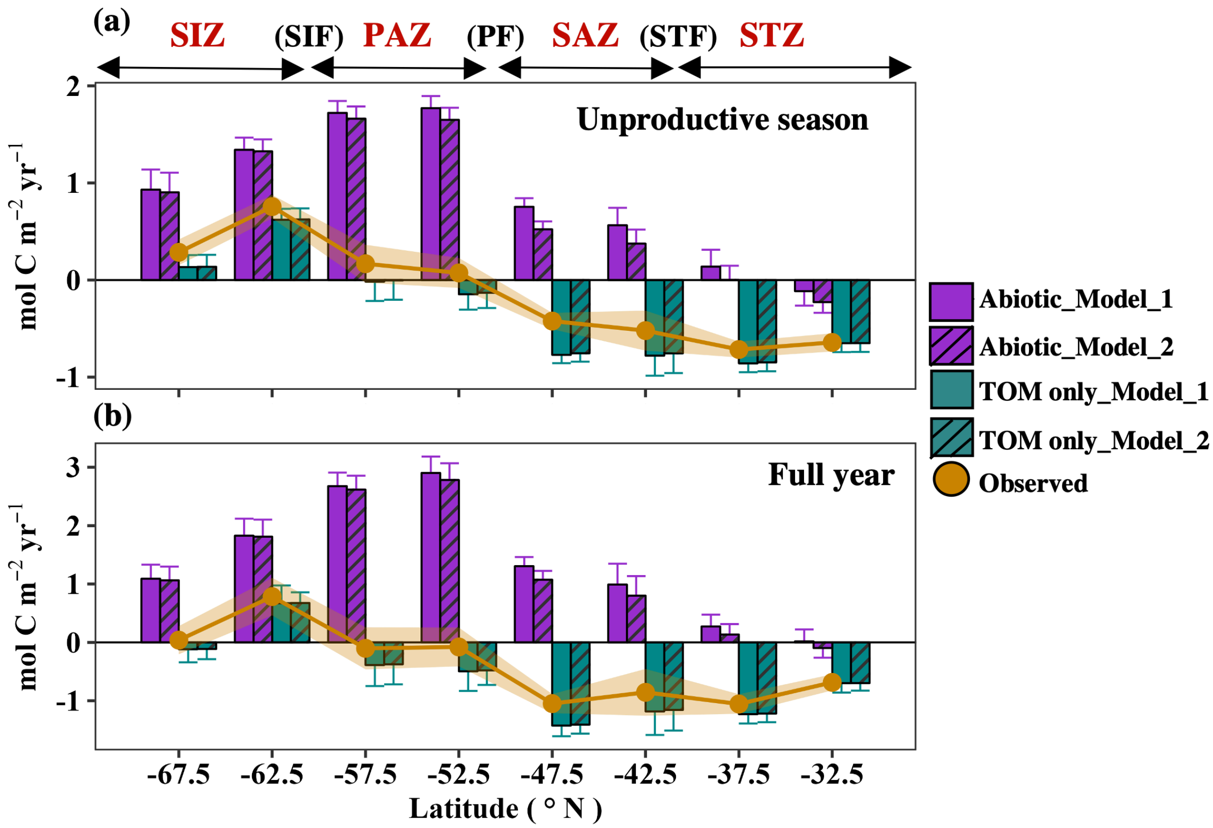

Fig. S10 Time cumulative air-sea CO_2 gas flux for different productivity scenarios during the (**a**) unproductive period and (**b**) the full year based on the different model settings. Gold lines show the observed CO_2 fluxes. Frontal zones as described in **Fig. S1**. Positive values indicate a source of carbon to the atmosphere. Error bars and shading represent the propagated uncertainty in each scenario. Model 1 (adopted in the main text): reconstruction results the abiotic and TOM production only scenarios in which the unproductive season contributes to the total annual production (***Materials and Methods*** in main text); Model 2: reconstruction results the abiotic and TOM production only scenarios in which the unproductive season does not contribute to the total annual production.

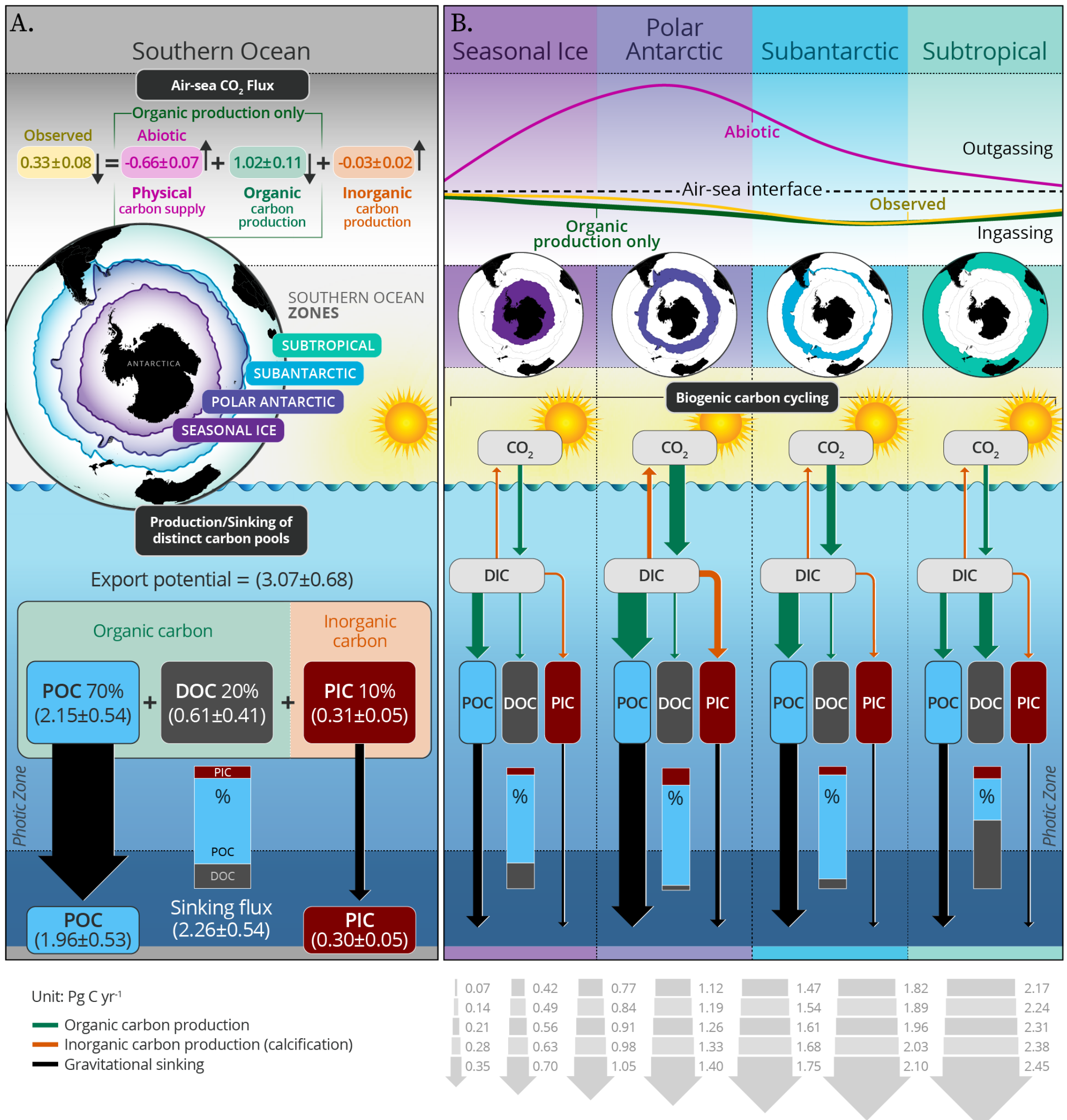

Fig. S11 Schematic of Southern Ocean carbon cycling during the productive season. Contributions of distinct biogenic carbon pools to the total biological carbon production and the associated impacts on air-sea CO_2 flux. Arrow sizes are proportional to the area-weighted, cumulative carbon flux magnitude within each frontal zone. Inset bar plots show the percentage contributions of each biogenic carbon pool to the export potential.

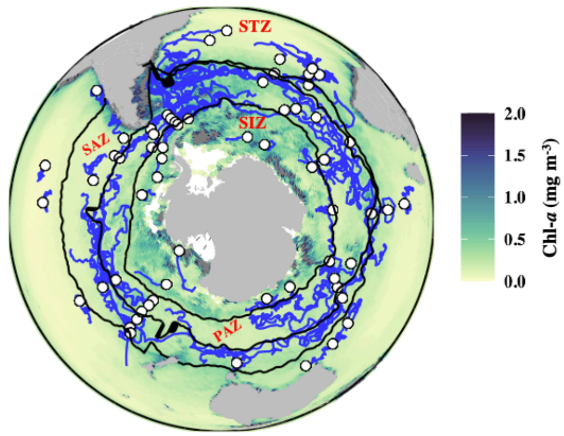

Fig. S12 Trajectories of the floats used in this study. White dots show the deployment locations. The background color shows a climatology of remotely sensed surface chlorophyll-*a* during austral summer. Black lines show the climatological boundaries (mean of 2004–2014) of the Southern Ocean fronts determined using an Argo-based climatology of temperature and salinity (32). Zones as described in **Fig. S1**.

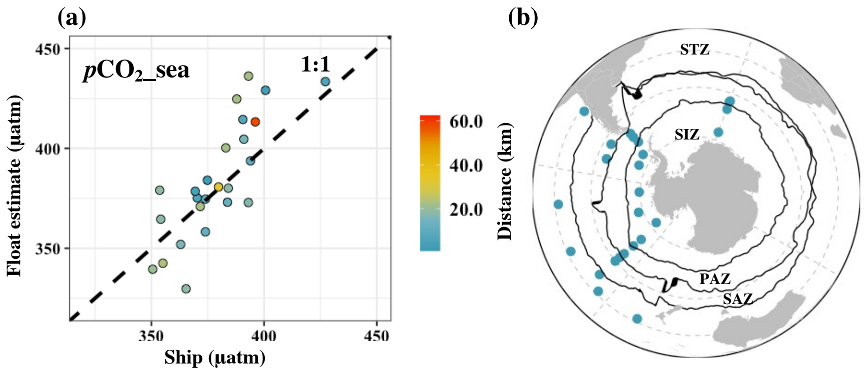

Fig. S13 (a) Comparison of the sea surface partial pressure of carbon dioxide ($p\text{CO}_{2\_\text{sea}}$) from float estimates and underway shipboard observations compiled in SOCAT (version 2022 (33)). **(b)** The float and ship samples were paired based on location (±0.2°) and sampling date (±2 days). The color bar in **a** reflects the distance between ship and float samples. Frontal zones in panel b as described in **Fig. S1**.

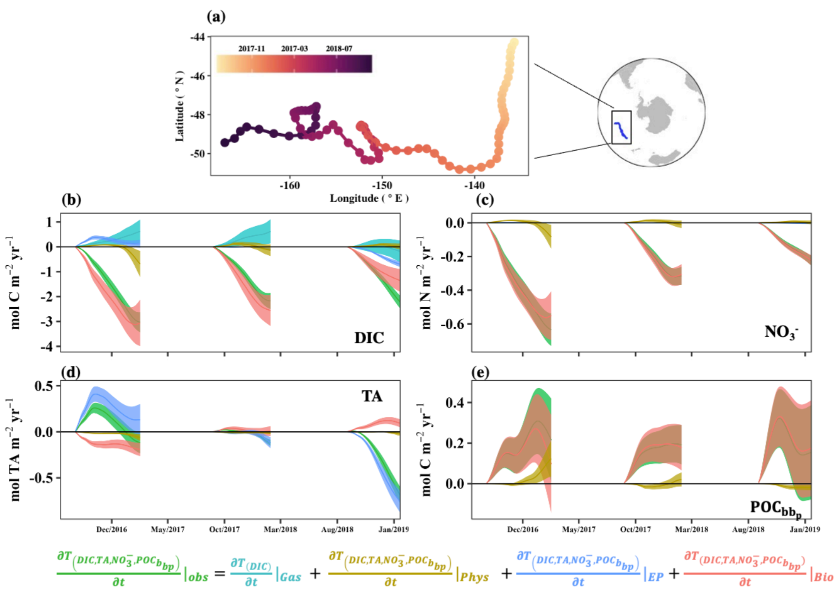

Fig. S14 Time cumulative fluxes in each productive season within the euphotic zone (~77m) for a representative biogeochemical float (WMO ID: 5904761). Shading represents the propagated error. Positive values indicate the process causes an increase in the tracer inventory. DIC: dissolved inorganic carbon; NO_3^-: nitrate; TA: total alkalinity; $POC_{b_{bp}}$: particulate organic carbon derived from the backscattering coefficient.

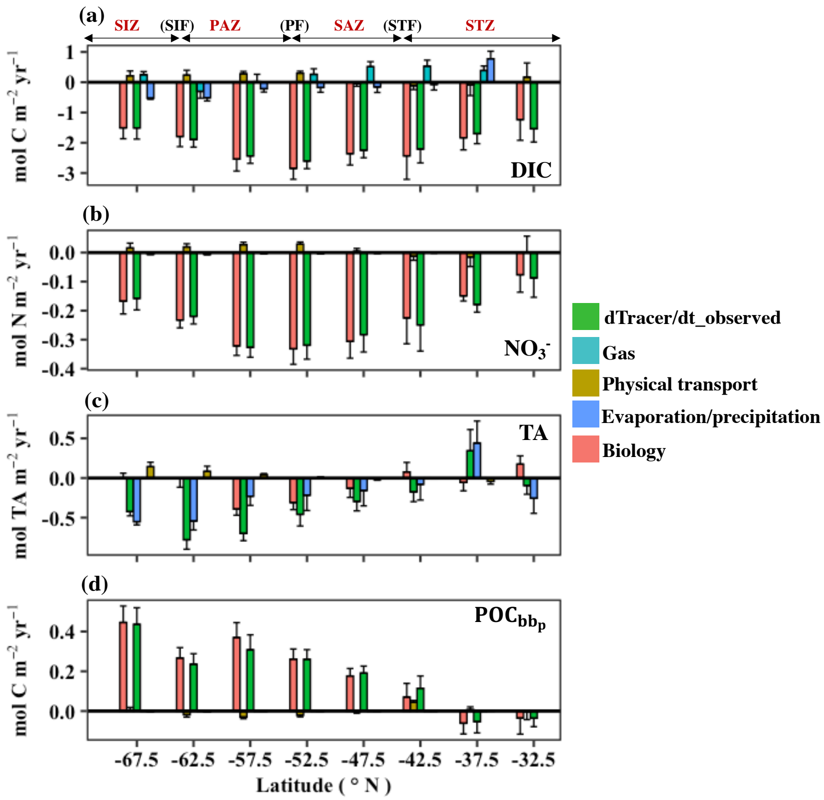

Fig. S15 Meridional pattern (5° bin) of tracer budget integrated over the euphotic zone during the Southern Ocean productive season. Error bars represent the propagated error. The positive value indicates the process leads to an increase in the tracer inventory. DIC: dissolved inorganic carbon; NO_3^-: nitrate; TA: total alkalinity; $POC_{b_{bp}}$: particulate organic carbon derived from the backscattering coefficient. Zones as described in **Fig. S1**.

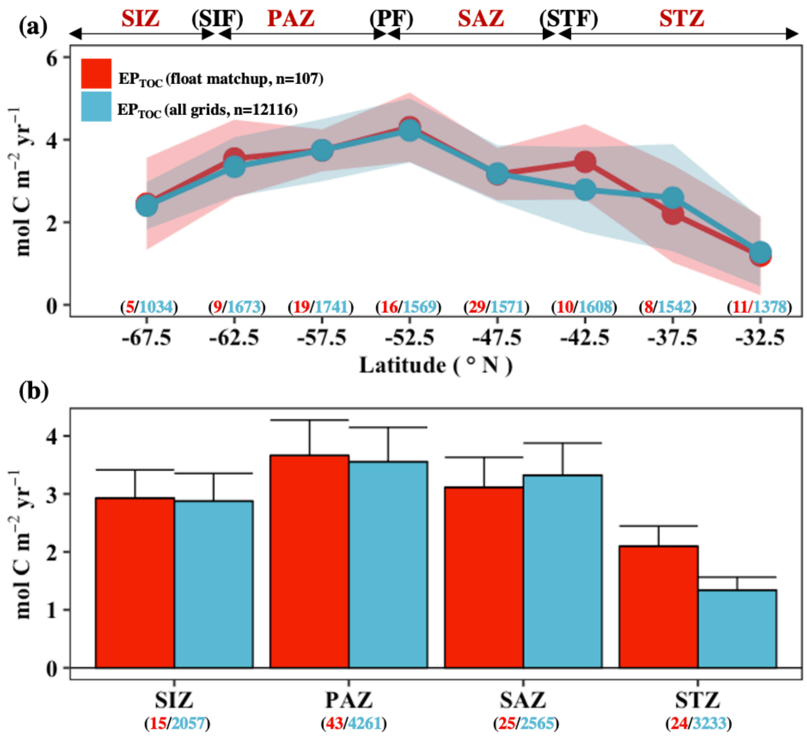

Fig. S16 Evaluation, using data constrained biogeochemical Southern Ocean State Estimate (B-SOSE) model output (31), of how representative the float-based productivity estimates are of the entire Southern Ocean. Comparison of subsampled (along float trajectories) versus fully resolved (1°×1°) model fields of euphotic zone integrated export potential of total organic carbon (E_{TOC}) during the productive season. Results are shown as an average (**a**) across meridional bands and (**b**) the four main frontal regions. Shading and error bars reflect spatial variability in EP_{TOC} within each sub-region. Red and blue numbers near the bottom of each panel show the number of grid points used in each sub-region for computing the average value. The frontal regions are as described in **Fig. S1**.

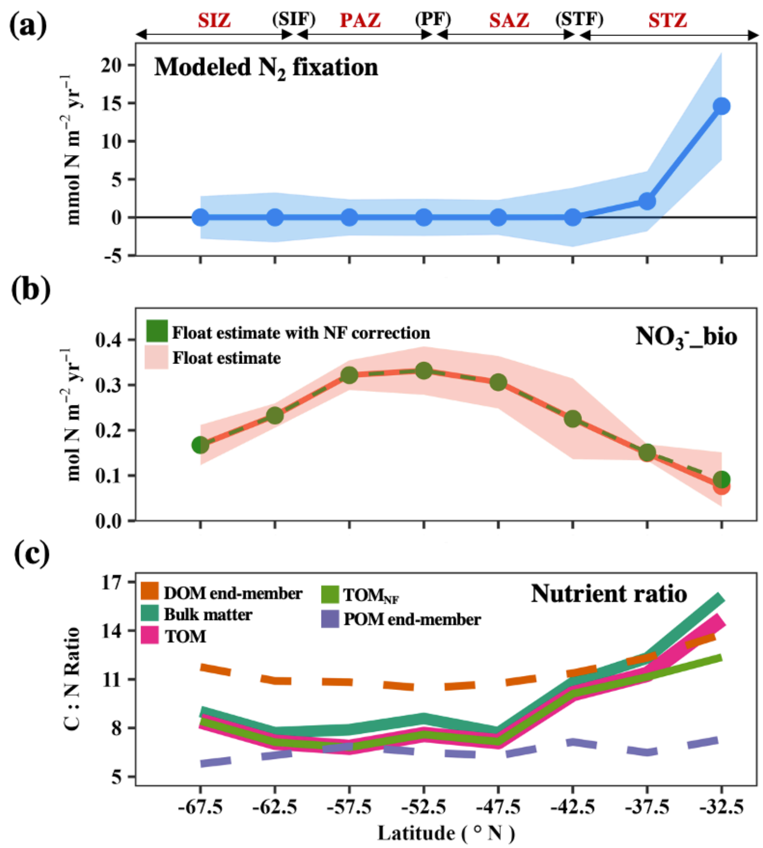

Fig. S17 The meridional pattern of (**a**) climatology of nitrogen fixation (NF) derived from a data-driven inverse model (34), and (**b**) net biological term solved from nitrate tracer budget ($NO_3^-{}_{\text{-bio}}$), **(c)** carbon-to-nitrogen ratios (C:N) for biological production of different carbon pools during the Southern Ocean productive season. The dissolved organic matter (DOM) and particulate organic matter (POM) end-member C:N ratios are derived from the compilation of existing ship-based observations. The bulk biological production, total organic matter (TOM) production, and TOM production with the correction for nitrogen fixation (TOM_{NF}) are derived from float observations and a biogeochemical inverse model. Shading on each line reflects the propagated error. Zones as described in **Fig. S1**.

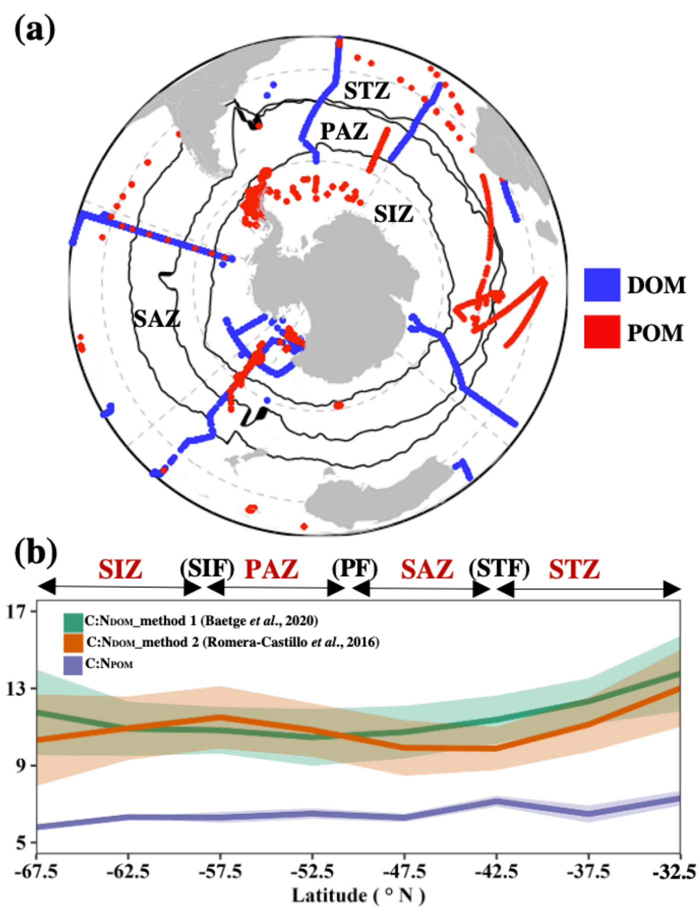

Fig. S18 (**a**) Distribution of discrete particulate organic matter (POM) and dissolved organic matter (DOM) observations and the (**b**) meridional patterns of end-member C:N ratios for POM ($C:N_{POM}$) and DOM ($C:N_{DOM}$) produced during the Southern Ocean productive season. Shading represents the propagated error. Zones as described in **Fig. S1**. $C:N_{DOM}$_method 1 and $C:N_{DOM}$_method 2 represent the results from two different approaches described in **Text S1.1**.

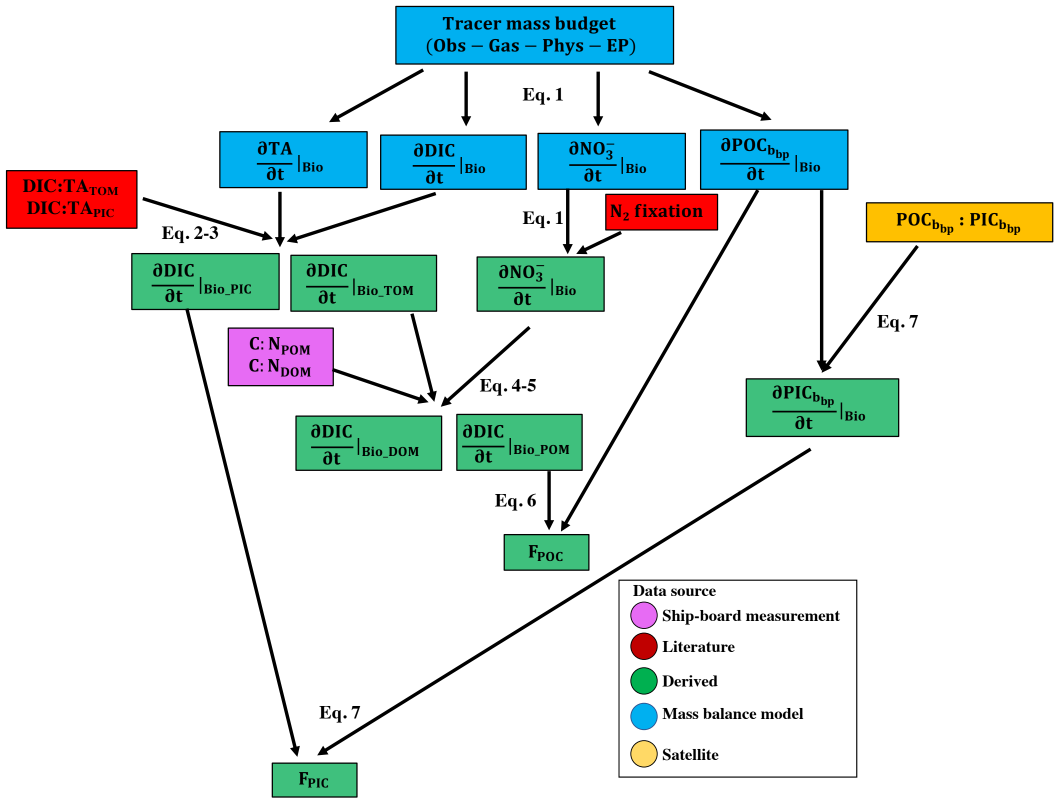

Fig. S19 A schematic to depict the workflow and data sources for multiple terms applied in distinct carbon pools partitioning. See detailed descriptions for each term in the method section.

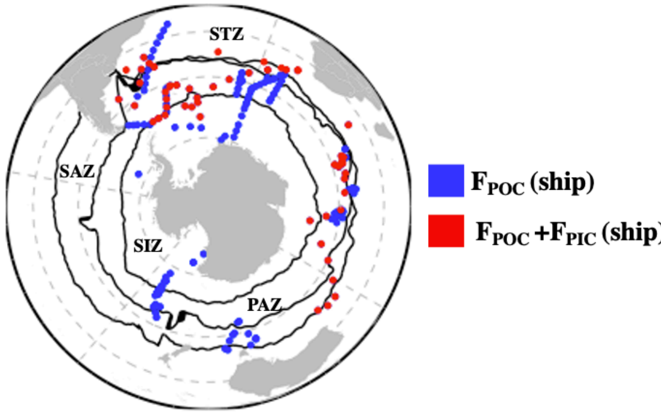

Fig. S20 Distribution of discrete particulate organic carbon (F_{POC}) and particulate inorganic carbon (F_{PIC}) sinking fluxes inferred from measurements of ^{234}Th-^{238}U disequilibrium during the Southern Ocean productive seasons. See **Text S1.2** for a detailed description of the flux calculation and integration adjustment. Zones as described in **Fig. S1**.

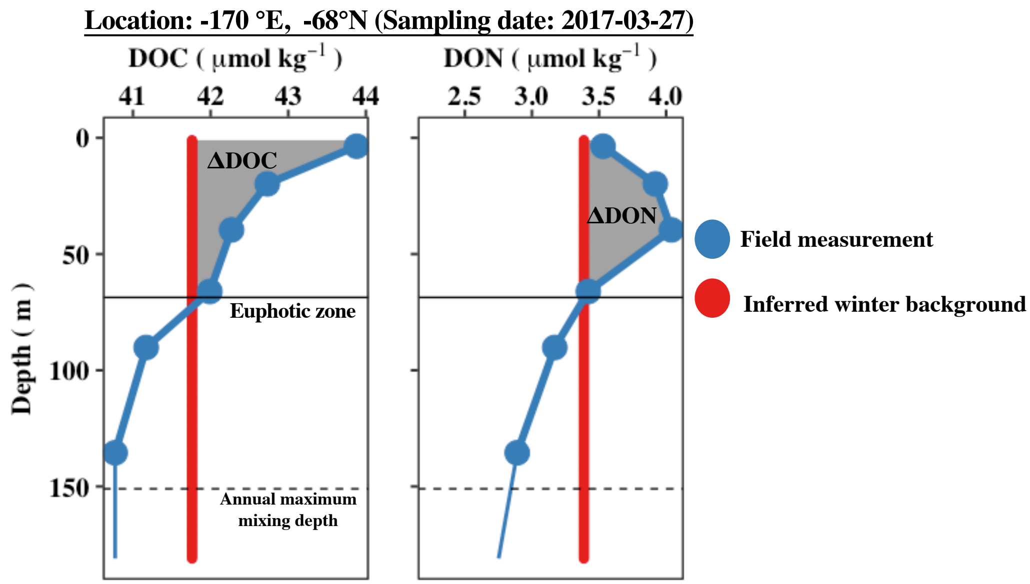

Fig. S21 An example illustrating the reconstruction of seasonal dissolved organic matter (ΔDOM) production ratios based on profiles of dissolved organic carbon (DOC) and dissolved organic nitrogen (DON) collected during the stratified summer. Method following Baetge*, et al.* (2).

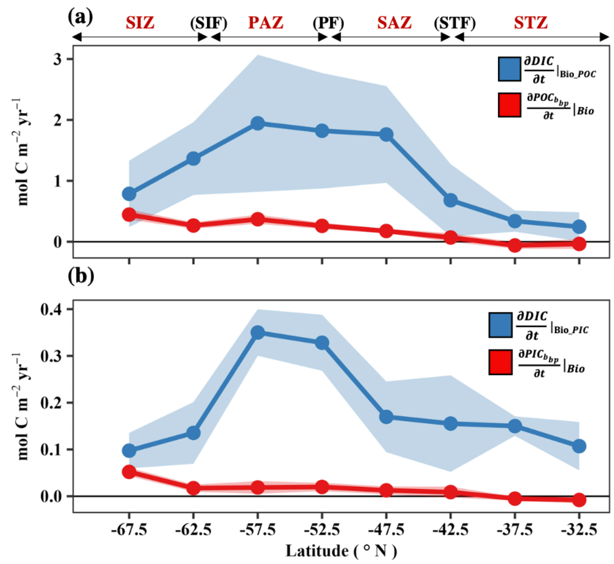

Fig. S22 Meridional pattern (5° bin) of euphotic zone net biological terms solved from suspended particles ($\frac{\partial \mathrm{POC}_{\mathrm{b_{bp}}}}{\partial \mathrm{t}}|_{\mathrm{Bio}}$ and $\frac{\partial \mathrm{PIC}_{\mathrm{b_{bp}}}}{\partial \mathrm{t}}|_{\mathrm{Bio}}$) and the DIC tracer budget ($\frac{\partial \mathrm{DIC}}{\partial \mathrm{t}}|_{\mathrm{Bio\_POC}}$ and $\frac{\partial \mathrm{DIC}}{\partial \mathrm{t}}|_{\mathrm{Bio\_PIC}}$) during the Southern Ocean productive season. Shading reflects the propagated error. Zones as described in **Fig. S1**. POC: particulate organic carbon; PIC: particulate inorganic carbon.

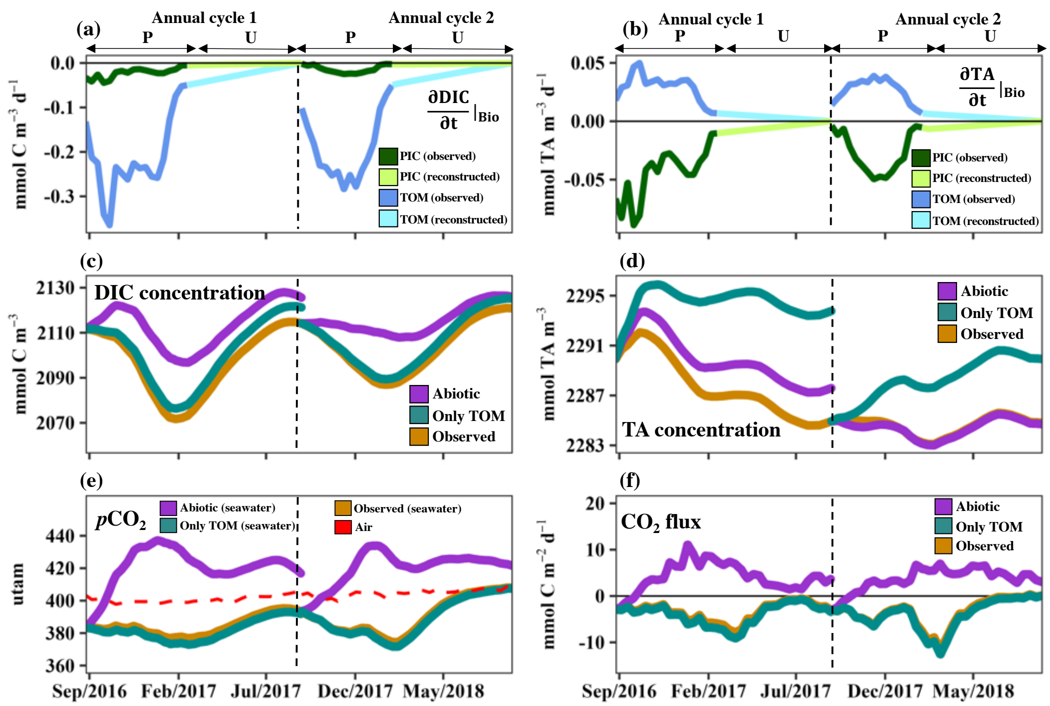

Fig. S23 Time-series of (**a**) biologically-induced dissolved inorganic carbon (DIC) change, (**b**) biologically-induced total alkalinity (TA) change, **(c)** DIC concentration, **(d)** TA concentration, **(e)** partial pressure of carbon dioxide (pCO_2), and (**f**) air-sea CO_2 gas flux over two annual cycles for a representative biogeochemical float (WMO ID: 5904761) under three different productivity scenarios: observed, abiotic, and total organic matter production only. Reconstructions of productivity during the unproductive (U) period are based on the fraction of total production occurring during the productive (P) period in B-SOSE model output (***Materials and* Methods** in main text).

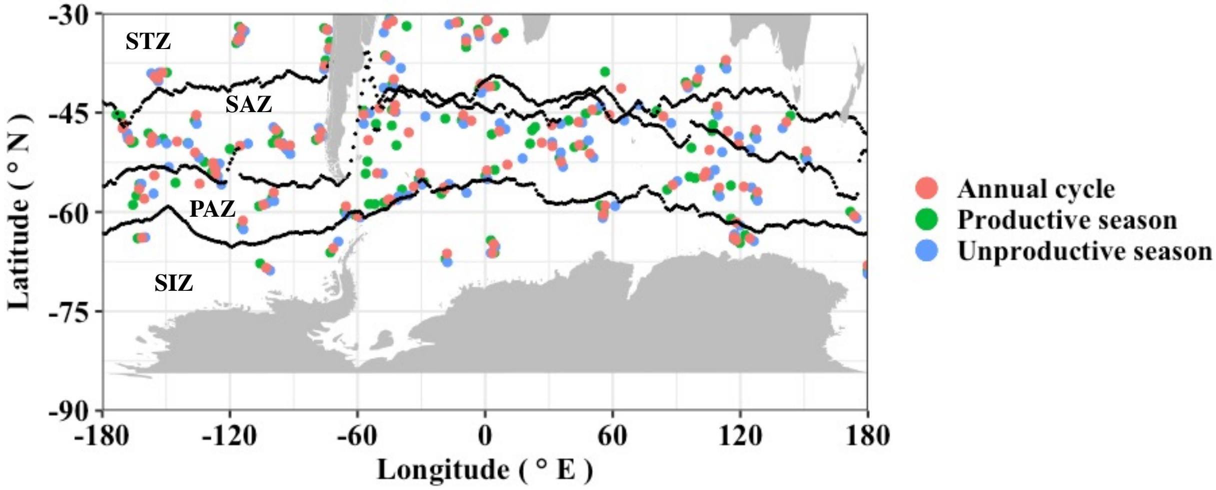

Fig. S24 Mean location of each float during each annual cycle, productive season, or unproductive season. Black lines show the climatological locations (mean of 2004–2014) of Southern Ocean fronts determined using an Argo-based climatology of temperature and salinity (32). Zones as described in **Fig. S1**.

Table S1. List of World Meteorological Organization identification numbers (WMO IDs) for the biogeochemical floats used in this study.

No.	WMO ID	No.	WMO ID	No.	WMO ID	No.	WMO ID
1	5904188	21	5904686	41	5905135	61	5906244
2	5904395	22	5904693	42	5905981	62	5906245
3	5904396	23	5904695	43	5905982	63	5906250
4	5904468	24	5904761	44	5905995		
5	5904469	25	5904765	45	5905996		
6	5904470	26	5904766	46	5905997		
7	5904473	27	5904768	47	5905998		
8	5904657	28	5904842	48	5906003		
9	5904658	29	5904844	49	5906007		
10	5904659	30	5904854	50	5906031		
11	5904660	31	5904856	51	5906032		
12	5904661	32	5904857	52	5906204		
13	5904662	33	5904980	53	5906208		
14	5904663	34	5904982	54	5906209		
15	5904673	35	5905075	55	5906211		
16	5904675	36	5905105	56	5906216		
17	5904679	37	5905109	57	5906218		
18	5904682	38	5905131	58	5906222		
19	5904683	39	5905132	59	5906224		
20	5904684	40	5905134	60	5906227		

Table S2 Assignment of uncertainties used in the Monte Carlo error analysis. NO_3^-: nitrate; TA: total alkalinity; $POC_{b_{bp}}$: particulate organic carbon based on backscattering coefficient; Chl-*a*: Chlorophyll-*a* concentration based on Chlorophyll-fluorescence; CO_2: carbon dioxide; MLD: mixed layer depth; POM: particulate organic matter; DOM: dissolved organic matter.

Variable	Uncertainty	Reference
pH measurement	±0.005	Johnson, *et al.* (35)
NO_3^- measurement	±0.5 μmol kg^{-1}	Johnson, *et al.* (20)
TA estimates	± 4.5 μmol kg^{-1}	Bittig, *et al.* (11)
$POC_{b_{bp}}$ estimates	±30%	Graff, *et al.* (36)
Chl-*a* estimates	20%	Johnson, *et al.* (20)
CO_2 gas model	±30%	Bender, *et al.* (25), Wanninkhof (26)
Background eddy diffusivity coefficient	±35%	Yang, *et al.* (23)
Ekman pumping velocity	±50%	Haskell, *et al.* (37)
Thickness of MLD	±0.5 m	Vertical resolution/4
Thickness of euphotic zone	5-15 m	Spatial variability at each latitude band (**Fig. S1a**)
C:N ratio for POM/DOM production	0.5-2.5	Spatial variability at each latitude band (**Fig. S18a**)
Model-simulated N_2 fixation	10-30%	Spatial variability at each latitude band (**Fig. S17a**)

Table S3 Summary of ancillary parameters used in this study.

Parameters	Description	Reference /Link	Usage
Parameters used to partition carbon pools and in tracer budget closure			
Ice coverage	Monthly surface ice coverage; 25 km resolution	Global Sea Ice Concentration Climate Data (https://cds.climate.copernicus.eu/cdsapp#!/dataset/satellite-sea-ice-concentration?tab=overview)	Scale the air-sea CO_2 exchange by ice fraction
Euphotic zone depth (Zeu)	Remote-sensed daily surface property. MODIS; 083°×0. 083°; Level 3	Ocean color (https://oceandata.sci.gsfc.nasa.gov/directdataaccess/Level-3%20Mapped/Aqua-MODIS)	Determine the Zeu
Wind stress	Daily surface wind stress; 0.25° × 0. 25°	Advanced Scatterometer product (https://manati.star.nesdis.noaa.gov/datasets/ASCATData.php)	Calculate the Ekman pumping velocity
Wind speed	Daily values; 0.16 °×0.16°	NCEP-DOE reanalysis: II (https://psl.noaa.gov/data/gridded/data.ncep.reanalysis2.html)	Calculate the atmospheric pCO_2 and air-sea CO_2 fluxes
Air pressure			
Relative humidity			
N_2 fixation	Monthly climatology simulated from inverse biogeochemical and prognostic ocean models; 1°×1°; 24 depth interval	Wang, *et al.* (34)	Correct NO_3^- potential export
Particulate inorganic carbon (PIC)	Daily surface properties; 083°×0. 083°; Level 3	Ocean color (https://oceandata.sci.gsfc.nasa.gov/directdataaccess/Level-3%20Mapped/Aqua-MODIS)	Derive the PIC:POC ratio to estimate seawater PIC inventory
Particulate organic carbon (POC)			
Dissolved organic matter (DOM)	Global compilation of dissolved organic carbon (DOC) and dissolved organic nitrogen (DON=total dissolved nitrogen – total inorganic nitrogen) observations	Hansell et al., (2021) (https://www.ncei.noaa.gov/access/metadata/landing-page/bin/iso?id=gov.noaa.nodc:0227166)	Constrain the end-member C:N ratio of DOM and POM produced
Particulate organic matter (POM)	Global compilation of suspended particulate organic carbon (POC) and particulate organic nitrogen (PON) observations	Martiny, *et al.* (38) (https://www.bco-dmo.org/dataset/526747)	
Parameters used to validate or compare with float analysis			
Particulate organic/inorganic carbon sinking flux (F_{POC}/F_{PIC})	Compilation of POC and PIC sinking fluxes inferred from ^{2234}Th-^{238}U	Henson, *et al.* (5), Le Moigne, *et al.* (6), Rosengard, *et al.* (7)	Compare with the float estimate
Export potential of organic carbon	Monthly climatology (2013-2021); 016°×0.16°	Biogeochemical Southern Ocean State Estimate (B-SOSE) (http://sose.ucsd.edu/) (31)	Evaluate the representativeness of the spatial variability of carbon export derived from the float locations
Parameters used to analyze light and nutrient availability			

Dissolved iron (dFe) concentration	Monthly climatology simulated from a data-driven model; 1°×1°; 33 depth interval	Huang, *et al.* (12) (https://zenodo.org/record/6994318#.Y0m2fuzMLjk)	Analyze the meridional pattern of dFe
SiO_4^- concentration	Estimated from float temperature, salinity, and dissolved oxygen observations	Canyon-B algorithm (11)	Analyze the meridional pattern of SiO_4^- dependent growth rate
Photosynthetically available radiation (PAR)	Remote-sensed daily surface properties; MODIS; 083°×0. 083°; Level 3	Ocean color (https://oceandata.sci.gsfc.nasa.gov/directdataaccess/Level-3%20Mapped/Aqua-MODIS)	Analyze the meridional pattern of light availability

References

1. D. A. Hansell, M. V. Orellana, Dissolved organic matter in the global ocean: A primer. *Gels* **7** (2021).
2. N. Baetge, J. R. Graff, M. J. Behrenfeld, C. A. Carlson, Net community production, dissolved organic carbon accumulation, and vertical export in the western North Atlantic. *Frontiers in Marine Science* **7** (2020).
3. J. Holte, L. D. Talley, J. Gilson, D. Roemmich, An Argo mixed layer climatology and database. *Geophysical Research Letters* **44**, 5618-5626 (2017).
4. C. Romera-Castillo, R. T. Letscher, D. A. Hansell, New nutrients exert fundamental control on dissolved organic carbon accumulation in the surface Atlantic Ocean. *Proceedings of the National Academy of Sciences* **113**, 10497-10502 (2016).
5. S. Henson, F. Le Moigne, S. Giering, Drivers of carbon export efficiency in the global ocean. *Global Biogeochem Cycles* **33**, 891-903 (2019).
6. F. A. Le Moigne, K. Pabortsava, C. L. Marcinko, P. Martin, R. J. Sanders, Where is mineral ballast important for surface export of particulate organic carbon in the ocean? *Geophys Res Lett* **41**, 8460-8468 (2014).
7. S. Z. Rosengard *et al.*, Carbon export and transfer to depth across the Southern Ocean Great Calcite Belt. *Biogeosciences* **12**, 3953-3971 (2015).
8. J. H. Martin, G. A. Knauer, D. M. Karl, W. W. Broenkow, VERTEX: carbon cycling in the northeast Pacific. *Deep-Sea Res* **34**, 267-285 (1987).
9. W. M. Balch *et al.*, Factors regulating the Great Calcite Belt in the Southern Ocean and its biogeochemical significance. *Global Biogeochemical Cycles* **30**, 1124-1144 (2016).
10. I. Salter *et al.*, Carbonate counter pump stimulated by natural iron fertilization in the Polar Frontal Zone. *Nature Geoscience* **7**, 885-889 (2014).
11. H. C. Bittig *et al.*, An alternative to static climatologies: robust estimation of open ocean CO_2 variables and nutrient concentrations from T, S, and O_2 data using Bayesian Neural Networks. *Frontiers in Marine Science* **5** (2018).
12. Y. Huang, A. Tagliabue, N. Cassar, Data-driven modeling of dissolved iron in the global ocean. *Frontiers in Marine Science* **9** (2022).
13. A. R. Gray *et al.*, Autonomous biogeochemical floats detect significant carbon dioxide outgassing in the high-latitude Southern Ocean. *Geophysical Research Letters* **45**, 9049-9057 (2018).
14. S. M. Bushinsky *et al.*, Reassessing Southern Ocean air-Sea CO_2 flux estimates with the addition of biogeochemical float observations. *Global Biogeochem Cycles* **33**, 1370-1388 (2019).
15. S. Stammerjohn *et al.*, Antarctica and the Southern Ocean. *Bulletin of the American Meteorological Society* **102**, S317-S356 (2021).
16. P. Landschützer, N. Gruber, D. C. E. Bakker, Decadal variations and trends of the global ocean carbon sink. *Global Biogeochemical Cycles* **30**, 1396-1417 (2016).
17. P. Landschützer, N. Gruber, D. C. E. Bakker, U. Schuster, Recent variability of the global ocean carbon sink. *Global Biogeochemical Cycles* **28**, 927-949 (2014).
18. C. J. Prend *et al.*, Indo-Pacific Sector Dominates Southern Ocean Carbon Outgassing. *Global Biogeochemical Cycles* **36** (2022).
19. M. C. Long *et al.*, Strong Southern Ocean carbon uptake evident in airborne observations. *Science* **374**, 1275-1280 (2021).

20. K. S. Johnson *et al.*, Biogeochemical sensor performance in the SOCCOM profiling float array. *Journal of Geophysical Research: Oceans* **122**, 6416-6436 (2017).
21. C. de Boyer Montégut, G. Madec, A. S. Fischer, A. Lazar, D. Iudicone, Mixed layer depth over the global ocean: an examination of profile data and a profile-based climatology. *Journal of Geophysical Research-Oceans* **109**, C12003 (2004).
22. S. R. Signorini, C. R. McClain, J. R. Christian, C. S. Wong, Seasonal and interannual variability of phytoplankton, nutrients, TCO_2, pCO_2, and O_2 in the eastern subarctic Pacific (ocean weather station Papa). *Journal of Geophysical Research: Oceans* **106**, 31197-31215 (2001).
23. B. Yang, S. R. Emerson, S. M. Bushinsky, Annual net community production in the subtropical Pacific Ocean from *in-situ* oxygen measurements on profiling floats. *Global Biogeochemical Cycles* **31**, 728–744 (2017).
24. O. M. Sun, S. R. Jayne, K. L. Polzin, B. A. Rahter, L. C. St. Laurent, Scaling turbulent dissipation in the transition layer. *Journal of Physical Oceanography* **43**, 2475-2489 (2013).
25. M. L. Bender, S. Kinter, N. Cassar, R. Wanninkhof, Evaluating gas transfer velocity parameterizations using upper ocean radon distributions. *Journal of Geophysical Research: Oceans* **116** (2011).
26. R. Wanninkhof, Relationship between wind speed and gas exchange over the ocean revisited. *Limnology and Oceanography: Methods* **12**, 351-362 (2014).
27. B. R. Carter, J. A. Radich, H. L. Doyle, A. G. Dickson, An automated system for spectrophotometric seawater pH measurements. *Limnology and Oceanography: Methods* **11**, 16-27 (2013).
28. N. L. Williams *et al.*, Calculating surface ocean pCO_2 from biogeochemical Argo floats equipped with pH: An uncertainty analysis. *Global Biogeochemical Cycles* **31**, 591-604 (2017).
29. B. R. Carter *et al.*, Updated methods for global locally interpolated estimation of alkalinity, pH, and nitrate. *Limnology and Oceanography: Methods* **16**, 119-131 (2018).
30. A. Morel *et al.*, Examining the consistency of products derived from various ocean color sensors in open ocean (Case 1) waters in the perspective of a multi-sensor approach. *Remote Sensing of Environment* **111**, 69-88 (2007).
31. A. Verdy, M. R. Mazloff, A data assimilating model for estimating Southern Ocean biogeochemistry. *Journal of Geophysical Research: Oceans* **122**, 6968-6988 (2017).
32. D. Roemmich, J. Gilson, The 2004–2008 mean and annual cycle of temperature, salinity, and steric height in the global ocean from the Argo Program. *Progress in Oceanography* **82**, 81-100 (2009).
33. D. C. E. Bakker *et al.*, A multi-decade record of high-quality fCO_2 data in version 3 of the Surface Ocean CO_2 Atlas (SOCAT). *Earth System Science Data* **8**, 383-413 (2016).
34. W. L. Wang, J. K. Moore, A. C. Martiny, F. W. Primeau, Convergent estimates of marine nitrogen fixation. *Nature* **566**, 205-211 (2019).
35. K. S. Johnson *et al.*, Deep-Sea DuraFET: A pressure tolerant pH sensor designed for global sensor networks. *Analytical chemistry* **88**, 3249-3256 (2016).
36. J. R. Graff *et al.*, Analytical phytoplankton carbon measurements spanning diverse ecosystems. *Deep Sea Research Part I: Oceanographic Research Papers* **102**, 16-25 (2015).

37. W. Z. Haskell, A. J. Fassbender, J. S. Long, J. N. Plant, Annual net community production of particulate and dissolved organic carbon from a decade of biogeochemical profiling float observations in the Northeast Pacific. *Global Biogeochemical Cycles* **34** (2020).
38. A. C. Martiny, J. A. Vrugt, M. W. Lomas, Concentrations and ratios of particulate organic carbon, nitrogen, and phosphorus in the global ocean. *Sci Data* **1**, 140048 (2014).